

# Effects of Repetitive Pressure on the Photoluminescence of Bare and ZnS-Capped CuInS<sub>2</sub> Quantum Dots: Implications for Nanoscale Stress Sensors

Jundiao Wang,<sup>1</sup> Haoran Ning,<sup>1</sup> Jun Wang, Stephen V. Kershaw, Lihong Jing,\* and Pan Xiao\*



Cite This: ACS Appl. Nano Mater. 2022, 5, 5617–5624



Read Online

ACCESS |

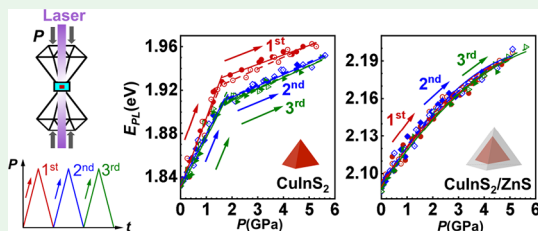
Metrics & More

Article Recommendations

Supporting Information

**ABSTRACT:** Semiconductor quantum dots (QDs) are promising materials for stress/strain sensing applications owing to their pressure-dependent photoluminescence (PL) and nanoscale size, while the impact of stress and microstructure on their optical properties still awaits in-depth investigations under more realistic loading conditions. Herein, bare CuInS<sub>2</sub> QDs and core-shell structured CuInS<sub>2</sub>/ZnS QDs are investigated under repetitive pressure loadings to elucidate the pressure-dependent PL responses over many pressure cycles. The CuInS<sub>2</sub>/ZnS QDs not only show higher PL intensity but also exhibit a reliable and simple relationship between PL emission peak energy ( $E_{PL}$ ) and external pressure ( $P$ ), which is desirable for actual application in stress/strain sensing. Specifically, the  $E_{PL}$ – $P$  relationship of bare CuInS<sub>2</sub> QDs changes after the first loading–unloading cycle, while the  $E_{PL}$ – $P$  relationship of CuInS<sub>2</sub>/ZnS QDs shows repeatable trajectories under different cycles. This research provides experimental support for designing QD-based stress/strain sensing materials and explains how the shell and surface microstructure will affect the mechanical-luminescence responses of QDs.

**KEYWORDS:** CuInS<sub>2</sub> quantum dots, core–shell structure, repetitive loading, stress/strain sensing, photoluminescence properties



## INTRODUCTION

Quantum dots (QDs) are appealing nanoscale stress/strain sensing materials (SSMs) because of their small size, high photoluminescence (PL) intensity, and tunable band gap governed by the quantum confinement effect.<sup>1–6</sup> For example, the potential of QDs applied to detect the pressure induced by explosion, shock, or extreme conditions in experimental biology is enormous due to their GPa-level pressure-sensitive merits.<sup>7–9</sup> Moreover, QDs can also be employed for in situ stress/strain detection in highly heterogeneous materials because of their nanometer size.<sup>5</sup> Based on the potential of QDs for stress/strain sensing, the PL responses of QDs related to external pressure under several loading conditions have been studied over the past few years. Because a majority of QDs are synthesized by liquid phase-based chemical approaches, most related reports focus on the PL of QDs under hydrostatic compression conditions.<sup>10–14</sup> It is reported that in most cases, hydrostatic compression leads to a blueshift of the PL,<sup>11,12,14</sup> which can be used as an indicator for pressure sensing. However, the PL often disappears when it is loaded to a critical pressure regime.<sup>8,15</sup> Phase transformation is the most possible reason accounting for the disappearance of the PL, and thus, many efforts have been put into the underlying phase transition mechanism of QDs through both experimental<sup>16–19</sup> and theoretical methods.<sup>20</sup> In addition, QDs as SSMs under shock compression<sup>1,5</sup> and uniaxial compression<sup>21–25</sup> have also been investigated recently. In comparison with the PL

response in hydrostatic compression, a nonmonotonic dependence between the PL peak shift and external pressure is observed in both shock compression and uniaxial compression experiments due to the axiality of stress states and the crystal orientation of the QDs,<sup>1,23,24</sup> which would lead to inaccurate pressure sensing performance.

Although the research on QDs under different pressure loading conditions has provided valuable information for developing QD-based SSMs, there still remains much work to be done for more realistic conditions. For example, the pressure-dependent PL response of QD-based SSMs has to be repeatable under repeated loading–unloading cycles for long-term experiments, and stress/strain sensors are usually used in dynamic systems. However, studies on the PL response of QDs under such repeated loading–unloading cycles are less common. Moreover, because the direct chemical synthesis of core–shell QDs becomes mature, research on the mechanical properties of QDs is no longer limited to bare QDs. Core–shell QDs represent several advantages over bare QDs in terms

Received: February 7, 2022

Accepted: March 23, 2022

Published: April 5, 2022



of performance and structure, such as, enhanced PL to start with;<sup>26–31</sup> being less susceptible to interfering effects like oxidation;<sup>32</sup> and higher phase transition pressures.<sup>33</sup> Nevertheless, the impact of repetitive pressure loading on the PL properties of core–shell QDs still remains to be mapped out. Such a study would trigger further developments in the QD-based sensing field under more realistic conditions.

Following our previous works on the synthesis of semiconductor QDs<sup>34–36</sup> and considering the advantages of CuInS<sub>2</sub> QDs such as safety, stability, and pressure-sensitivity in the GPa-level,<sup>8</sup> herein, we report the repetitive pressure loading effects on the PL emission properties of both bare CuInS<sub>2</sub> QDs and the counterparts, core–shell structured CuInS<sub>2</sub>/ZnS QDs. Two important optical parameters, in terms of PL emission intensity and emission peak energy, were particularly investigated to elucidate the PL response behaviors of these QDs under more realistic pressure loading conditions. It was demonstrated that QDs after shell coating exhibited a more reliable and simple relationship between PL emission peak energy and external pressure during pressure loading–unloading cycles. We further discuss the role of the shell and surface microstructure governing the mechanical-luminescence response of QDs.

## EXPERIMENTAL METHODS

**Chemicals.** Indium acetate [In(OAc)<sub>3</sub>, 99.99%] was purchased from Alfa Aesar. 1-Dodecanethiol (DDT, 98%) was purchased from Macklin. Copper(I) iodide (CuI, 99.95%) and zinc stearate (ZnSt<sub>2</sub>, 90%) were purchased from Aladdin. Acetone, cyclohexane, ethanol, and toluene were of analytical reagent grade and purchased from Sinopharm Chemical Reagent Beijing, Co., Ltd.

**Synthesis of Bare CuInS<sub>2</sub> QDs.** The CuInS<sub>2</sub> QDs were synthesized by a previously reported method,<sup>37</sup> as illustrated in Figure 1. In brief, 0.2 mmol In(OAc)<sub>3</sub> and 0.2 mmol CuI were mixed

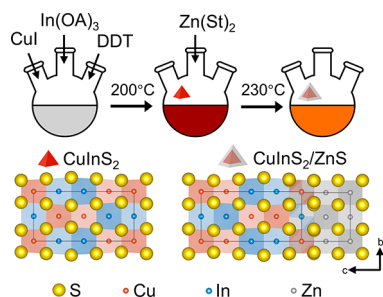


**Figure 1.** Scheme of synthesis approaches and structures of CuInS<sub>2</sub> and CuInS<sub>2</sub>/ZnS QDs.

with 12 mL of DDT. The mixture was first degassed under vacuum at 80 °C for 30 min until it turned into a clear solution. Then, the solution was purged with nitrogen and heated to 200 °C. The reaction was allowed to stand for 60 min under nitrogen protection. The resulting CuInS<sub>2</sub> QDs were precipitated by acetone and isolated by centrifugation, redispersed in cyclohexane, and subsequently precipitated by using acetone for three cycles. The QDs finally obtained were redispersed in toluene for further pressure loading experiments.

**Synthesis of Core–Shell CuInS<sub>2</sub>/ZnS QDs.** Following the aforementioned procedures for synthesizing bare CuInS<sub>2</sub> QDs, a parallel reaction mixture was prepared by 60 min reaction at 200 °C. Thereafter, 0.5 mmol ZnSt<sub>2</sub> was introduced at room temperature without applying the purification procedures to the mixture. The mixture was degassed under vacuum at 120 °C for 30 min and then purged with nitrogen gas. The resultant reaction mixture was heated to 230 °C and kept at that temperature for 60 min. The purification

procedures for the CuInS<sub>2</sub>/ZnS QDs were the same as those of the bare CuInS<sub>2</sub> QDs mentioned above.

**Hydrostatic Pressure Loading Experiments.** The hydrostatic pressure loading experiments were performed using a symmetric diamond anvil cell (DAC) with a culet size of 500 μm. Specifically, a gasket hole with a diameter of 400 μm served as a sample chamber for sealing a toluene solution of QDs in the anvil. The element concentrations of QDs are listed in Table S1. A small ruby particle was also put into the cavity for pressure calibration. Two loading modes were applied to QDs from the same samples. In the first mode, QDs in the DAC were loaded quasistatically to a critical pressure ( $P_{cr}$ ) until the emission of the QDs disappeared. In the second mode, in order to prevent the emission from disappearing, loading–unloading cycles were performed with a suitable maximum pressure less than  $P_{cr}$ . In both modes, PL spectra were recorded by a spectrometer with the probe keeping at almost the same distance from the sample.

**Characterization.** The transmission electron microscopy (TEM) images were obtained on a JEM-2100F electron microscope operating at an accelerating voltage of 200 kV. The powder X-ray diffraction (XRD) patterns were recorded on a Bruker D2 Phaser X-ray diffractometer at 150 mA with Cu K $\alpha$  radiation. PL spectra were recorded at room temperature on an Aurora4000 fluorescence spectrophotometer equipped with a 405 nm laser as a single wavelength excitation source (15 mW). The absolute PL quantum yield (PLQY) measurement was performed on an Edinburgh FLS980 spectrometer equipped with an integrating sphere upon 350 nm excitation and calculated from the number of emitted photons per absorbed photons. The chemical composition and concentration of the two QD samples were determined by inductively coupled plasma-atomic emission spectrometry (ICP-AES) using ICP-AES 6300DV after the decomposition of QD particles with a concentrated nitric acid.

## RESULTS AND DISCUSSION

Representative TEM images of the bare CuInS<sub>2</sub> and CuInS<sub>2</sub>/ZnS QDs together with their particle size distribution profiles are shown in Figure 2a,b. The average diameter of the CuInS<sub>2</sub> QDs is increased from  $1.5 \pm 0.4$  to  $2.6 \pm 0.6$  nm upon ZnS coating, which supports the formation of an outer ZnS shell with a thickness of around 0.55 nm. The ZnS shell overcoated on the surface of the CuInS<sub>2</sub> core is also supported by the fact that the relative standard deviation of the particle size is decreased from 26.7 to 23.1% after ZnS shell growth. The actual Cu/In ratios of the CuInS<sub>2</sub> and CuInS<sub>2</sub>/ZnS QD samples were determined to be 1 (Table S1), in accordance with the stoichiometric ratio in CuInS<sub>2</sub>. The well-resolved powder XRD patterns shown in Figure 2c further confirm the preservation of the chalcopyrite (tetragonal) phase structure characteristic of the CuInS<sub>2</sub> core throughout the ZnS shell-coating process.<sup>38</sup> The lattice constants for CuInS<sub>2</sub> are  $a = b = 5.517$  Å and  $c = 11.06$  Å, while they are  $a = b = c = 5.345$  Å for ZnS with a zinc blende phase. The intrinsic lattice mismatch between them is about 3% that is low enough to allow for epitaxial shell growth.<sup>39,40</sup> To further investigate the shell coating effects on the PL properties under pressure loading, bare CuInS<sub>2</sub> and core–shell CuInS<sub>2</sub>/ZnS QDs were separately put into the gasket cavity together with a ruby particle (for pressure calibration), as illustrated in Figure 2d. Pressure is then applied when bringing the anvils together by controlling the spring gasket. PL spectra are recorded by a spectrometer with the detector at a fixed distance from the samples loaded for monitoring the PL emission properties under pressure.

The PL spectra of CuInS<sub>2</sub> and CuInS<sub>2</sub>/ZnS QDs at different pressure levels after the first pressure loading are presented in Figure 3a,b, respectively. Obviously, the pressure-dependent PL intensities for two samples are not monotonically varying,

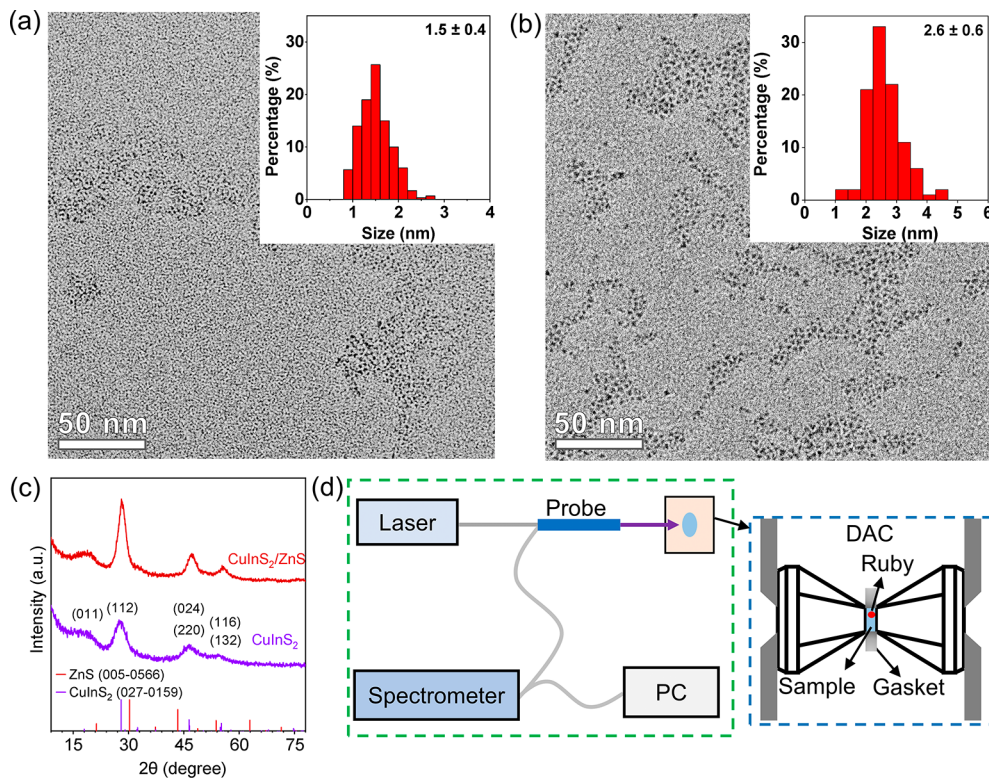


**Figure 2.** Typical TEM images and the corresponding size histograms (inset) of (a) CuInS<sub>2</sub> and (b) CuInS<sub>2</sub>/ZnS QDs, together with (c) respective XRD patterns. (d) Experiment setup used for pressure loadings of QDs.

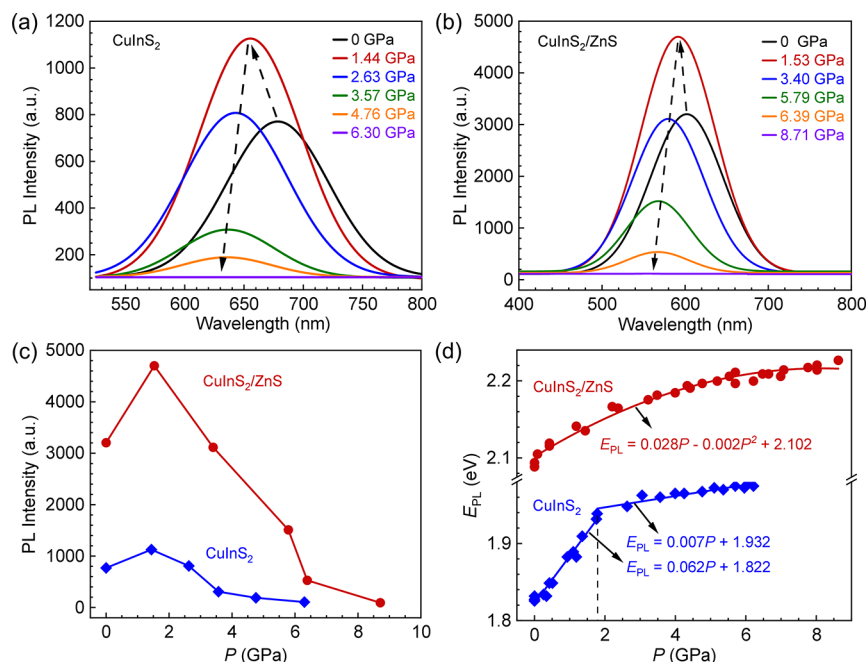


**Figure 3.** Pressure-dependent PL spectra of (a) CuInS<sub>2</sub> and (b) CuInS<sub>2</sub>/ZnS QDs. (c) Pressure-dependent PL intensity of CuInS<sub>2</sub> and CuInS<sub>2</sub>/ZnS QDs. (d) Pressure-dependent PL peak energy ( $E_{PL}$ ) of CuInS<sub>2</sub> and CuInS<sub>2</sub>/ZnS QDs (solid points) and fitting results (lines).

and therefore, the PL intensity as a function of pressure is further plotted in Figure 3c. The PL intensity of CuInS<sub>2</sub>/ZnS remains higher than that of the bare CuInS<sub>2</sub> QDs at the same pressure level. This can be attributed to the enhanced PLQY after performing the ZnS shelling process, that is, from 6.2% for bare CuInS<sub>2</sub> QDs to 20.2% for core–shell CuInS<sub>2</sub>/ZnS QDs, due to the efficient passivation via the ZnS shell and a

reduction of nonradiative recombination centers.<sup>41–43</sup> Upon pressure loading, it can be observed in both samples that the PL intensity increases with the external pressure at the beginning and similar characteristic has also been observed in InP/ZnS QDs,<sup>14</sup> which is directly related to the modulation of pressure on self-trapped exciton binding energy<sup>44</sup> and confined motion of the alkylthiol ligands. Thereafter, the PL intensity

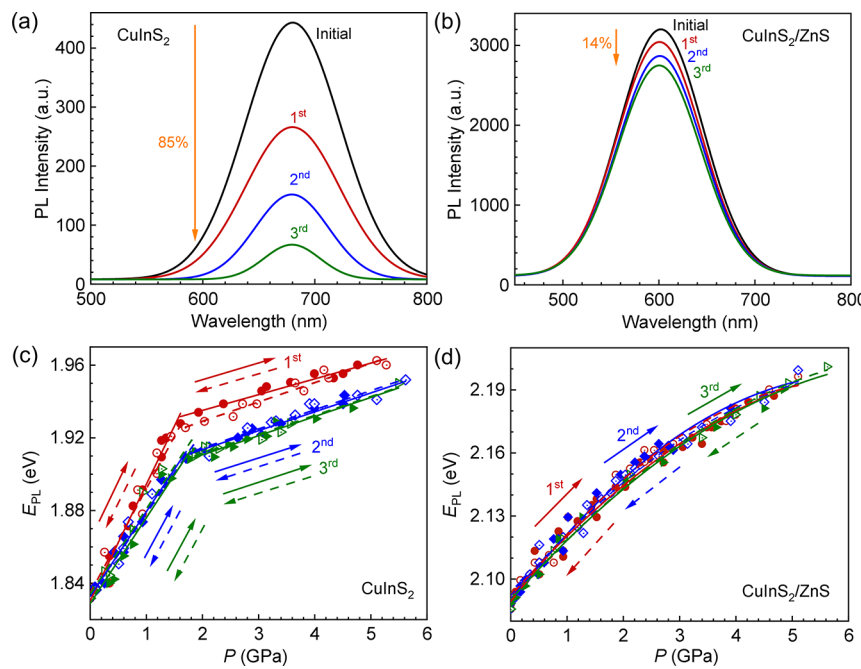


**Figure 4.** PL spectra after three loading–unloading cycles of (a) CuInS<sub>2</sub> and (b) CuInS<sub>2</sub>/ZnS QDs (the black curves represent the PL spectra of samples at the initial state; the red, blue, and green curves represent the spectra after the first, second, and third unloadings, respectively). PL peak energy evolution (symbols) and fitting results (lines) of (c) CuInS<sub>2</sub> and (d) CuInS<sub>2</sub>/ZnS QDs under three loading–unloading cycles. (Solid symbols/lines represent loading/fitting results. Open symbols/dashed lines represent unloaded/fitting results. Circle, square, and triangle symbols represent three load–unload cycles.)

decreases dramatically with pressure and disappears at a critical pressure ( $P_{\text{cr}}$ ). In the present experiments, the  $P_{\text{cr}}$  of CuInS<sub>2</sub> QDs is about 6.30 GPa, while it increases up to 8.71 GPa for CuInS<sub>2</sub>/ZnS QDs. It should be mentioned that the  $P_{\text{cr}}$  here is not corresponding to the pressure of the phase transition from chalcopyrite to cubic,<sup>19</sup> since it is smaller than that (9.6 GPa) of the phase transition pressure of bulk CuInS<sub>2</sub>.<sup>18,45–47</sup> The weakening of the PL intensity in the experiments is related to the distortion of the lattice and the QD-ligand bonding,<sup>8</sup> which leads to the trapping of photogenerated carriers and the weakening or even disappearance of the PL emission.<sup>15</sup> Moreover, at higher pressure levels, the decrease in PL intensity induced by the distortion is much larger than the increase in PL intensity by the modulation on self-trapped exciton binding energy and the confinement motion of ligands, and thus, it is observed that the PL intensity increases first and then decreases with pressure loading. In order to obtain sufficiently accurate data and avoid causing much larger lattice deformations of the QDs, the maximum pressure ( $P_{\text{max}}$ ) in the following repetitive pressure loading conditions is limited to about 5.50 GPa.

The evolution profiles of the PL peak energy (denoted as  $E_{\text{PL}}$ ) of CuInS<sub>2</sub> and CuInS<sub>2</sub>/ZnS QDs with the increasing pressure are presented in Figure 3d.  $E_{\text{PL}}$  is calculated from  $E_{\text{PL}} = hc/\lambda_{\text{max}}$ , where  $h$  is the Planck constant,  $c$  is the velocity of light, and  $\lambda_{\text{max}}$  is the wavelength at the peak maxima of PL spectra.  $E_{\text{PL}}$  is directly related to the band gap energy of QDs, which is governed by the quantum confinement effect.<sup>48,49</sup> Diameter and lattice spacing of QDs decrease due to the external pressure, which in turn enhances the quantum confinement and leads to the increase in band gap energy.<sup>49,50</sup> As a result,  $E_{\text{PL}}$  increases with the loading pressure. However,  $E_{\text{PL}}$  for the two types of QDs show different pressure

dependencies. Specifically, a bilinear model can be used to fit the pressure-dependent  $E_{\text{PL}}$  of CuInS<sub>2</sub> QDs<sup>14,50</sup>

$$E_{\text{PL}} = \begin{cases} \alpha_L P + E_{0L} & P < P_{\text{tr}} \\ \alpha_H P + E_{0H} & P \geq P_{\text{tr}} \end{cases} \quad (1)$$

where  $P_{\text{tr}}$  is the turning point of the bilinear model,  $\alpha_L$  and  $E_{0L}$  are fitting parameters in the low pressure regime, and  $\alpha_H$  and  $E_{0H}$  are fitting parameters in the high pressure regime.  $E_{0L}$  is the fitted extrapolated PL peak energy of the CuInS<sub>2</sub> QDs at zero pressure. For the CuInS<sub>2</sub>/ZnS QDs, a quadratic function is more suitable for fitting the  $E_{\text{PL}}-P$  relationship<sup>12,14,50</sup>

$$E_{\text{PL}} = \alpha P + \beta P^2 + E_0 \quad (2)$$

where  $\alpha$  and  $\beta$  are the first-order and second-order coefficients obtained by fitting, respectively, and  $E_0$  is the fitted PL peak energy at zero pressure. The functions and related coefficients can be utilized as a reference for pressure sensing in experiments. The parameters obtained by fitting the two models are given in Figure 3d. It can be seen that  $P_{\text{tr}}$  for CuInS<sub>2</sub> QDs is about 1.76 GPa. The slope before  $P_{\text{tr}}$  of CuInS<sub>2</sub> QDs is 0.062 eV/GPa, which is much larger than that (0.007 eV/GPa) after  $P_{\text{tr}}$ . As for CuInS<sub>2</sub>/ZnS QDs, the initial slope at a lower pressure level is about 0.028 eV/GPa, which is less than that of CuInS<sub>2</sub> QDs. It is worth noting that although the core size of the two types of QDs in experiments is similar,  $E_{\text{PL}}$  of CuInS<sub>2</sub>/ZnS QDs at ambient pressure is about 2.102 eV, which is larger than 1.822 eV of CuInS<sub>2</sub> QDs. This difference is mainly caused by the combined effects of surface passivation by ZnS as well as the shrinking of the CuInS<sub>2</sub> core.<sup>41</sup>

For the repetitive pressure loading conditions, the PL spectra after three loading–unloading cycles with  $P_{\text{max}} = 5.50$  GPa are recorded and presented in Figure 4a,b. The PL intensity of both bare and core–shell QDs decreases with

pressure loading cycles but by different degrees. When reaching the third pressure loading–unloading cycles, the PL intensity of CuInS<sub>2</sub>/ZnS QDs is decreased only by a total of 14%, which is significantly less than that of CuInS<sub>2</sub> QDs (85%). As discussed above, QD-ligand bonds can be distorted or even broken under pressure, whereas the broken bonds are difficult to recover, as described by Liu et al.,<sup>8</sup> leading to a continuous weakening in PL intensity of CuInS<sub>2</sub> QDs with the increasing number of loading–unloading cycles. However, for the core–shell-structured CuInS<sub>2</sub>/ZnS QDs, the weakening of PL spectra is mainly caused by the lattice distortion at the interface, which can be almost recovered after unloading due to the low lattice mismatch (~3%) between CuInS<sub>2</sub> and ZnS.<sup>8</sup> As a result, the weakening of the PL intensity of CuInS<sub>2</sub>/ZnS QDs is much lower than that of CuInS<sub>2</sub> QDs after three loading–unloading cycles. The PL intensity of CuInS<sub>2</sub>/ZnS QDs remains higher than that of CuInS<sub>2</sub> QDs regardless of the repeated pressure loading cycles, benefiting from the higher starting PLQY of the core–shells.

The pressure-dependent  $E_{PL}$  values of CuInS<sub>2</sub> and CuInS<sub>2</sub>/ZnS QDs under different loading–unloading cycles are further shown in Figure 4c,d, respectively, together with the corresponding fitting parameters that are listed in Tables 1

**Table 1.** Fitting Parameters in Figure 4c

cycle		$\alpha_L$ (eV/GPa)	$\alpha_H$ (eV/GPa)	$E_{0L}$ (eV)	$E_{0H}$ (eV)
1st	load	0.064	0.009	1.830	1.918
	unload	0.058	0.010	1.835	1.907
2nd	load	0.047	0.010	1.833	1.893
	unload	0.045	0.010	1.833	1.893
3rd	load	0.047	0.011	1.829	1.890
	unload	0.047	0.010	1.834	1.891

**Table 2.** Fitting Parameters in Figure 4d

cycle		$\alpha$ (eV/GPa)	$\beta$ (eV/GPa <sup>2</sup> )	$E_0$ (eV)
1st	load	0.030	-0.002	2.092
	unload	0.035	-0.003	2.089
2nd	load	0.035	-0.003	2.089
	unload	0.031	-0.002	2.092
3rd	load	0.030	-0.002	2.090
	unload	0.031	-0.002	2.089

and 2. The  $P_{max}$  of each loading–unloading cycle is kept close to 5.50 GPa, as described above. The variations of  $E_{PL}$ – $P$  relations of CuInS<sub>2</sub> and CuInS<sub>2</sub>/ZnS QDs with pressure

loading–unloading cycles are quite distinct. For CuInS<sub>2</sub> QDs, as shown in Figure 4c, the first loading and unloading trajectories basically coincide with each other, and  $E_{PL}$  returns to the initial value when fully unloaded. Similar behaviors have also been observed in InP/ZnS and CuInS<sub>2</sub> QDs in other works.<sup>8,14</sup> However, the  $E_{PL}$  of the second loading trajectory becomes smaller than that of the first loading trajectory at the same pressure level. The fitting slopes  $\alpha_L$  and  $\alpha_H$  can characterize the pressure sensitivity of QDs in different pressure regions.  $\alpha_L$  decreases by 26.6% from 0.064 to 0.047 eV/GPa, while  $\alpha_H$  remains nearly unchanged (Table 1). Therefore, the smaller  $E_{PL}$  after  $P_{tr}$  is due to the decrease in  $\alpha_L$ . After that, the subsequent unloading and loading trajectories generally coincide with the second loading trajectory. It can be noted that the  $P_{tr}$  of all the trajectories is similar and close to 1.76 GPa, which will be discussed later. In contrast, it is obvious that the  $E_{PL}$ – $P$  trajectories of the CuInS<sub>2</sub>/ZnS QDs basically remain the same during the three loading–unloading cycles shown in Figure 4d (the fitting results are shown in Table 2) due to the suppression of a surface plastic deformation, which will be discussed later. The full width at half-maximum (fwhm) of PL spectra of the two samples is also pressure-dependent (Figure S1). For CuInS<sub>2</sub> QDs, the PL fwhm increases by 240, 188, and 128% after the first, second, and third loadings, respectively, indicating the broadening of PL spectra, which is similar to that of bare InP QDs.<sup>34</sup> However, the fwhm of CuInS<sub>2</sub>/ZnS QDs for all the three loadings decrease only about 5%, which is much smaller and similar to the results reported for CdSe/ZnS QDs.<sup>10</sup>

To investigate the mechanism of the decreased  $E_{PL}$  after the first cycle observed in CuInS<sub>2</sub> QDs, experiments with different  $P_{max}$  were performed and the results are shown in Figure 5. Because the  $E_{PL}$ – $P$  trajectories of the CuInS<sub>2</sub> QDs during the second and third loading–unloading cycles are basically the same, as shown in Figure 4c, we only performed two loading–unloading cycles. From Figure 5a, it is observed that when the  $P_{max}$  value of 1.50 GPa is applied, the first and second loading–unloading trajectories coincide with each other. In Figure 5b, when increasing the  $P_{max}$  up to 1.99 GPa, that is greater than  $P_{tr}$ , the  $E_{PL}$ – $P$  trajectory of the second cycle is significantly lower than that of the first cycle, similar to that shown in Figure 4c. Moreover, the CuInS<sub>2</sub> QDs were kept at ambient pressure for over 10 h after the first loading–unloading cycle and then continued the pressure loadings (Figure S2), showing the consistent results with that shown in Figure 4c.

The abovementioned complicated pressure-dependent  $E_{PL}$  under repetitive loading–unloading cycles of the CuInS<sub>2</sub> QDs presented in Figures 4c and 5b could be related to their surface

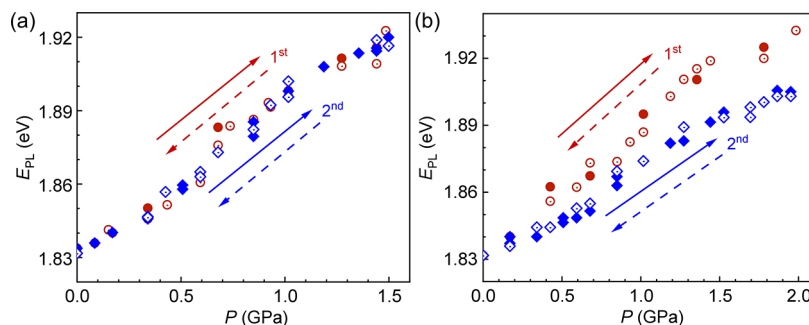


**Figure 5.** PL peak energy evolution of CuInS<sub>2</sub> QDs under repeated loading–unloading cycles with (a)  $P_{max} = 1.50$  GPa and (b)  $P_{max} = 1.99$  GPa.

and internal deformation<sup>51,52</sup> when applying high pressure. It can be understood from several perspectives:

- (1) Different mechanical properties of the surface and internal structure of bare CuInS<sub>2</sub> QDs lead to the bilinear model of the  $E_{PL}$ –P relationship. For the bare CuInS<sub>2</sub> QDs with nanoscale size, there is a strong surface energy, which leads to tangential tension pressure in the core due to a large surface-to-volume ratio.<sup>34,53</sup> Furthermore, as indicated in Figure 4c, slopes of the second and third loading–unloading cycles at low pressure regimes are smaller than that of the first loading–unloading cycle, but the slopes at the high pressure regime are basically independent of the times of the loading–unloading cycles. We therefore infer that the slope is mainly controlled by surface deformation in the low pressure regime and mainly by internal deformation in the high pressure regime. The turning pressure of these two deformation modes is close to  $P_{tr}$  as indicated in Figure 5. Moreover, the deformation on the surface is unrecoverable, as shown in Figure S2.
- (2) Plastic deformation occurs in the surface structure of bare CuInS<sub>2</sub> QDs after the first loading, which leads to the change of slope in the low pressure regime. Moreover, the plastic deformation strengthens the modulus of the surface layer (work hardening), and thus, the slope in the low-pressure regime decreases when the second loading is performed. However, there is no plastic deformation occurring in the internal region, and so, the slopes of the respective high-pressure regimes remain basically unchanged.
- (3) The ZnS shell of CuInS<sub>2</sub>/ZnS QDs can act as a protective layer for the underlying CuInS<sub>2</sub> core. In some regards, the ZnS shell coating is similar to the surface layer of CuInS<sub>2</sub> QDs in configuration, but only the internal CuInS<sub>2</sub> core deformation affects the PL behavior of CuInS<sub>2</sub>/ZnS QDs. That is to say, the  $E_{PL}$ –P relationship of the CuInS<sub>2</sub> core remains nearly unchanged regardless of any plastic deformation in the ZnS shell. Therefore, a single quadratic model can be used to fit the  $E_{PL}$ –P relationship, and it shows repeatable trajectories under different loading–unloading cycles.

## CONCLUSIONS

In summary, repetitive pressure loadings are applied to bare CuInS<sub>2</sub> QDs and core–shell CuInS<sub>2</sub>/ZnS QDs to disclose the pressure-dependent PL responses under more realistic conditions. It is demonstrated that core–shell CuInS<sub>2</sub>/ZnS QDs are more reliable as stress sensing nanomaterials in comparison with the bare CuInS<sub>2</sub> QDs for several perspectives. First, the PLQY of CuInS<sub>2</sub>/ZnS QDs in this case is higher than that of CuInS<sub>2</sub> QDs by a factor of approximately 3. Moreover, the decay of the PL intensity of the CuInS<sub>2</sub>/ZnS QDs due to the compression load is 20% of that of CuInS<sub>2</sub> QDs. Although it is inconvenient to use PL intensity as an indicator of pressure, the higher intensity and lower decay of the intensity can ensure sensitive response and a larger detection range for the spectrometer system employed. Second, the relationship between PL peak energy and the external pressure of CuInS<sub>2</sub>/ZnS QDs is simpler and more robust than that of CuInS<sub>2</sub> QDs. Obviously, the PL blueshift should be used as a pressure indicator when using QDs as SSMs given its monotonic

dependency. The quadratic fitting model of CuInS<sub>2</sub>/ZnS QDs is simpler than the bilinear model used for CuInS<sub>2</sub> QDs. Third, the structure of core/shell CuInS<sub>2</sub>/ZnS QDs is more stable during repeated pressure loadings in the pressure regime chosen. The ZnS shell can act as a protective layer for the CuInS<sub>2</sub> core, which not only renders the PL of CuInS<sub>2</sub>/ZnS QDs stronger and more stable but also is less prone to effects stemming from plastic deformation. As a result, under repetitive pressure loading–unloading cycles, CuInS<sub>2</sub>/ZnS QDs show a more stable and repeatable relationship between PL peak energy and external pressure. Therefore, the current study could in large perspective be extended to unfold the mechanical-luminescence responses of core–shell QDs, for the rational design of advanced QD-based stress/strain sensing nanomaterials.

## ASSOCIATED CONTENT

### Supporting Information

The Supporting Information is available free of charge at <https://pubs.acs.org/doi/10.1021/acsanm.2c00573>.

Pressure-dependent fwhm of two samples under three loading–unloading cycles; PL peak energy evolution with the pressure of CuInS<sub>2</sub> QDs obtained after the sample was left to stand for over 10 h after the first loading–unloading cycle; and molar concentration of each element in CuInS<sub>2</sub> and CuInS<sub>2</sub>/ZnS QDs ([PDF](#))

## AUTHOR INFORMATION

### Corresponding Authors

Lihong Jing – Key Laboratory of Colloid, Interface and Chemical Thermodynamics, Institute of Chemistry, Chinese Academy of Sciences, Beijing 100190, China;  [orcid.org/0000-0001-6115-2743](https://orcid.org/0000-0001-6115-2743); Email: [jinglh@iccas.ac.cn](mailto:jinglh@iccas.ac.cn); Fax: +86 10 8236 2540

Pan Xiao – State Key Laboratory of Nonlinear Mechanics, Institute of Mechanics, Chinese Academy of Sciences, Beijing 100190, China; Phone: +86 10 8254 3930; Email: [xiaopan@lnm.imech.ac.cn](mailto:xiaopan@lnm.imech.ac.cn)

### Authors

Jundiao Wang – State Key Laboratory of Nonlinear Mechanics, Institute of Mechanics, Chinese Academy of Sciences, Beijing 100190, China; School of Engineering Sciences, University of Chinese Academy of Sciences, Beijing 100049, China

Haoran Ning – Key Laboratory of Colloid, Interface and Chemical Thermodynamics, Institute of Chemistry, Chinese Academy of Sciences, Beijing 100190, China

Jun Wang – State Key Laboratory of Nonlinear Mechanics, Institute of Mechanics, Chinese Academy of Sciences, Beijing 100190, China

Stephen V. Kershaw – Department of Materials Science and Engineering & Centre for Functional Photonics, City University of Hong Kong, Kowloon 99077 Hong Kong SAR, China;  [orcid.org/0000-0003-0408-4902](https://orcid.org/0000-0003-0408-4902)

Complete contact information is available at:

<https://pubs.acs.org/10.1021/acsanm.2c00573>

### Author Contributions

<sup>1</sup>J.W. and H.N. contributed equally to this work.

### Notes

The authors declare no competing financial interest.

## ACKNOWLEDGMENTS

Supports from the National Natural Science Foundation of China (NSFC) (11790292, 11672298, and 22177115), the NSFC Basic Science Center Program for “Multiscale Problems in Nonlinear Mechanics” (11988102), the Youth Innovation Promotion Association CAS (2018042), and National Key Research Program of China (2018YFA0208800) are gratefully acknowledged.

## REFERENCES

- (1) Xiao, P.; Ke, F.; Bai, Y.; Zhou, M. Deformation-Induced Blueshift in Emission Spectrum of CdTe Quantum Dot Composites. *Composites, Part B* **2017**, *120*, 54–62.
- (2) Lee, J.; Kim, S.; Lee, J.; Yang, D.; Park, B. C.; Ryu, S.; Park, I. A Stretchable Strain Sensor Based on a Metal Nanoparticle Thin Film for Human Motion Detection. *Nanoscale* **2014**, *6*, 11932–11939.
- (3) Choi, C. L.; Koski, K. J.; Olson, A. C. K.; Alivisatos, A. P. Luminescent Nanocrystal Stress Gauge. *Proc. Natl. Acad. Sci. U.S.A.* **2010**, *107*, 21306–21310.
- (4) Ford, K. B.; Collins, M. K.; Ajami, N. E.; Dowds, D.; Mesyef, K.; Trovillion, J.; Al-Chaar, G.; Marsh, C. P. Optical Response to Low Applied Pressure in a Quantum Dot Nanocomposite. *Mater. Lett.* **2013**, *106*, 301–303.
- (5) Kang, Z.; Banishev, A. A.; Lee, G.; Scripka, D. A.; Breidenich, J.; Xiao, P.; Christensen, J.; Zhou, M.; Summers, C. J.; Dlott, D. D.; Thadhani, N. N. Exploration of CdTe Quantum Dots as Mesoscale Pressure Sensors via Time-Resolved Shock-Compression Photoluminescent Emission Spectroscopy. *J. Appl. Phys.* **2016**, *120*, 043107.
- (6) Dai, G.; Wang, L.; Cheng, S.; Chen, Y.; Liu, X.; Deng, L.; Zhong, H. Perovskite Quantum Dots Based Optical Fabry-Pérot Pressure Sensor. *ACS Photonics* **2020**, *7*, 2390–2394.
- (7) Picard, A.; Oger, P. M.; Daniel, I.; Cardon, H.; Montagnac, G.; Chervin, J.-C. A Sensitive Pressure Sensor for Diamond Anvil Cell Experiments up to 2GPa: FluoSpheres. *J. Appl. Phys.* **2006**, *100*, 034915.
- (8) Liu, H.; Yang, X.; Wang, K.; Wang, Y.; Wu, M.; Zuo, X.; Yang, W.; Zou, B. Pressure-Induced Multidimensional Assembly and Sintering of CuInS<sub>2</sub> Nanoparticles into Lamellar Nanosheets with Band Gap Narrowing. *ACS Appl. Nano Mater.* **2020**, *3*, 2438–2446.
- (9) Li, B.; Liu, W.; Zhu, X.; Lin, S.; Yang, Y.; Yang, Q.; Jin, P. Pressure-Dependent Photoluminescence of CdSe/ZnS Quantum Dots: Critical Point of Different Pressure Regimes. *Phys. Lett. A* **2019**, *383*, 1483–1486.
- (10) Fan, H. M.; Ni, Z. H.; Feng, Y. P.; Fan, X. F.; Kuo, J. L.; Shen, Z. X.; Zou, B. S. High pressure photoluminescence and Raman investigations of CdSe/ZnS core/shell quantum dots. *Appl. Phys. Lett.* **2007**, *90*, 021921.
- (11) Łach, P.; Karczewski, G.; Wojnar, P.; Wojtowicz, T.; Brik, M. G.; Kamińska, A.; Reszka, A.; Kowalski, B. J.; Suchocki, A. Pressure Coefficients of the Photoluminescence of the IIVI Semiconducting Quantum Dots Grown by Molecular Beam Epitaxy. *J. Lumin.* **2012**, *132*, 1501–1506.
- (12) Lin, Y.-C.; Chou, W.-C.; Susha, A. S.; Kershaw, S. V.; Rogach, A. L. Photoluminescence and Time-Resolved Carrier Dynamics in Thiol-Capped CdTe Nanocrystals under High Pressure. *Nanoscale* **2013**, *5*, 3400–3405.
- (13) Li, B.; Wen, X.; Li, R.; Wang, Z.; Clem, P. G.; Fan, H. Stress-Induced Phase Transformation and Optical Coupling of Silver Nanoparticle Superlattices into Mechanically Stable Nanowires. *Nat. Commun.* **2014**, *5*, 4179.
- (14) Liu, H.; Zhao, X.; Yang, X.; Wang, Y.; Wu, M.; Jiang, J.; Wu, G.; Yuan, K.; Sui, L.; Zou, B. Piezochromic luminescence in all-inorganic core-shell InP/ZnS nanocrystals via pressure-modulated strain engineering. *Nanoscale Horiz.* **2020**, *5*, 1233–1239.
- (15) Zhou, B.; Xiao, G.; Yang, X.; Li, Q.; Wang, K.; Wang, Y. Pressure-Dependent Optical Behaviors of Colloidal CdSe Nano-platelets. *Nanoscale* **2015**, *7*, 8835–8842.
- (16) Ji, M.; Wang, H.; Gong, Y.; Cheng, H.; Zheng, L.; Li, X.; Huang, L.; Liu, J.; Nie, Z.; Zeng, Q.; Xu, M.; Liu, J.; Wang, X.; Qian, P.; Zhu, C.; Wang, J.; Li, X.; Zhang, J. High Pressure Induced in Situ Solid-State Phase Transformation of Nonepitaxial Grown Metal@ Semiconductor Nanocrystals. *J. Phys. Chem. Lett.* **2018**, *9*, 6544–6549.
- (17) Wickham, J. N.; Herhold, A. B.; Alivisatos, A. P. Shape Change as an Indicator of Mechanism in the High-Pressure Structural Transformations of CdSe Nanocrystals. *Phys. Rev. Lett.* **2000**, *84*, 923–926.
- (18) Tolbert, S. H.; Alivisatos, A. P. Size Dependence of a First Order Solid-Solid Phase Transition: The Wurtzite to Rock Salt Transformation in CdSe Nanocrystals. *Science* **1994**, *265*, 373–376.
- (19) Li, Y.; Wang, Y.; Tang, R.; Wang, X.; Zhu, P.; Zhao, X.; Gao, C. Structural Phase Transition and Electrical Transport Properties of CuInS<sub>2</sub> Nanocrystals under High Pressure. *J. Phys. Chem. C* **2015**, *119*, 2963–2968.
- (20) Grünwald, M.; Lutker, K.; Alivisatos, A. P.; Rabani, E.; Geissler, P. L. Metastability in Pressure-Induced Structural Transformations of CdSe/ZnS Core/Shell Nanocrystals. *Nano Lett.* **2013**, *13*, 1367–1372.
- (21) Jiang, X.; Zhao, J.; Jiang, X. Tuning the Electronic and Optical Properties of Hydrogen-Terminated Si Nanocluster by Uniaxial Compression. *J. Nanopart. Res.* **2012**, *14*, 818.
- (22) Peng, X.-H.; Ganti, S.; Alizadeh, A.; Sharma, P.; Kumar, S. K.; Nayak, S. K. Strain-Engineered Photoluminescence of Silicon Nanoclusters. *Phys. Rev. B: Condens. Matter Mater. Phys.* **2006**, *74*, 035339.
- (23) Fischer, T.; Stöttinger, S.; Hinze, G.; Bottin, A.; Hu, N.; Basché, T. Single Semiconductor Nanocrystals under Compressive Stress: Reversible Tuning of the Emission Energy. *Nano Lett.* **2017**, *17*, 1559–1563.
- (24) Grant, C. D.; Crowhurst, J. C.; Hamel, S.; Williamson, A. J.; Zaitseva, N. Anomalous Photoluminescence in CdSe Quantum-Dot Solids at High Pressure Due to Nonuniform Stress. *Small* **2008**, *4*, 788–794.
- (25) Jiang, X.; Zhao, J.; Zhuang, C.; Wen, B.; Jiang, X. Mechanical and Electronic Properties of Ultrathin Nanodiamonds under Uniaxial Compressions. *Diamond Relat. Mater.* **2010**, *19*, 21–25.
- (26) Chen, B.; Pradhan, N.; Zhong, H. From Large-Scale Synthesis to Lighting Device Applications of Ternary I-III-VI Semiconductor Nanocrystals: Inspiring Greener Material Emitters. *J. Phys. Chem. Lett.* **2018**, *9*, 435–445.
- (27) Ning, J.; Duan, Z.; Kershaw, S. V.; Rogach, A. L. Phase-Controlled Growth of CuInS<sub>2</sub> Shells to Realize Colloidal CuInSe<sub>2</sub>/CuInS<sub>2</sub> Core/Shell Nanostructures. *ACS Nano* **2020**, *14*, 11799–11808.
- (28) Moodely, D.; Kowalik, P.; Bujak, P.; Pron, A.; Reiss, P. Synthesis, Photophysical Properties and Surface Chemistry of Chalcopyrite-Type Semiconductor Nanocrystals. *J. Mater. Chem. C* **2019**, *7*, 11665–11709.
- (29) Zang, H.; Li, H.; Makarov, N. S.; Velizhanin, K. A.; Wu, K.; Park, Y.-S.; Klimov, V. I. Thick-Shell CuInS<sub>2</sub>/ZnS Quantum Dots with Suppressed “Blinking” and Narrow Single-Particle Emission Line Widths. *Nano Lett.* **2017**, *17*, 1787–1795.
- (30) Zhong, H.; Bai, Z.; Zou, B. Tuning the Luminescence Properties of Colloidal I-III-VI Semiconductor Nanocrystals for Optoelectronics and Biotechnology Applications. *J. Phys. Chem. Lett.* **2012**, *3*, 3167–3175.
- (31) Xia, C.; Meeldijk, J. D.; Gerritsen, H. C.; de Mello Donega, C. Highly Luminescent Water-Dispersible NIR-Emitting Wurtzite CuInS<sub>2</sub>/ZnS Core/Shell Colloidal Quantum Dots. *Chem. Mater.* **2017**, *29*, 4940–4951.
- (32) Zhang, J.; Sun, W.; Yin, L.; Miao, X.; Zhang, D. One-pot synthesis of hydrophilic CuInS<sub>2</sub> and CuInS<sub>2</sub>-ZnS colloidal quantum dots. *J. Mater. Chem. C* **2014**, *2*, 4812–4817.
- (33) Lv, P.; Sun, Y.; Sui, L.; Ma, Z.; Yuan, K.; Wu, G.; Liu, C.; Fu, R.; Liu, H.; Xiao, G.; Zou, B. Pressure-Tuned Core/Shell

- Configuration Transition of Shell Thickness-Dependent CdSe/CdS Nanocrystals. *J. Phys. Chem. Lett.* **2020**, *11*, 920–926.
- (34) Jing, L.; Kershaw, S. V.; Kipp, T.; Kalytchuk, S.; Ding, K.; Zeng, J.; Jiao, M.; Sun, X.; Mews, A.; Rogach, A. L.; Gao, M. Insight into Strain Effects on Band Alignment Shifts, Carrier Localization and Recombination Kinetics in CdTe/CdS Core/Shell Quantum Dots. *J. Am. Chem. Soc.* **2015**, *137*, 2073–2084.
- (35) Jiao, M.; Huang, X.; Ma, L.; Li, Y.; Zhang, P.; Wei, X.; Jing, L.; Luo, X.; Rogach, A. L.; Gao, M. Biocompatible off-stoichiometric copper indium sulfide quantum dots with tunable near-infrared emission via aqueous based synthesis. *Chem. Commun.* **2019**, *55*, 15053–15056.
- (36) McHugh, K. J.; Jing, L.; Severt, S. Y.; Cruz, M.; Sarmadi, M.; Jayawardena, H. S. N.; Perkinson, C. F.; Larusson, F.; Rose, S.; Tomasic, S.; Graf, T.; Tzeng, S. Y.; Sugarman, J. L.; Vlasic, D.; Peters, M.; Peterson, N.; Wood, L.; Tang, W.; Yeom, J.; Collins, J.; Welkhoff, P. A.; Karchin, A.; Tse, M.; Gao, M.; Bawendi, M. G.; Langer, R.; Jaklenec, A. Biocompatible Near-Infrared Quantum Dots Delivered to the Skin by Microneedle Patches Record Vaccination. *Sci. Transl. Med.* **2019**, *11*, No. eaay7162.
- (37) Ding, K.; Jing, L.; Liu, C.; Hou, Y.; Gao, M. Magnetically Engineered Cd-Free Quantum Dots as Dual-Modality Probes for Fluorescence/Magnetic Resonance Imaging of Tumors. *Biomaterials* **2014**, *35*, 1608–1617.
- (38) Li, L.; Pandey, A.; Werder, D. J.; Khanal, B. P.; Pietryga, J. M.; Klimov, V. I. Efficient Synthesis of Highly Luminescent Copper Indium Sulfide-Based Core/Shell Nanocrystals with Surprisingly Long-Lived Emission. *J. Am. Chem. Soc.* **2011**, *133*, 1176–1179.
- (39) Voigt, D.; Bredol, M.; Gonabadi, A. A General Strategy for CuInS<sub>2</sub> Based Quantum Dots with Adjustable Surface Chemistry. *Opt. Mater.* **2021**, *115*, 110994.
- (40) Li, L.; Daou, T. J.; Texier, I.; Kim Chi, T. T.; Liem, N. Q.; Reiss, P. Highly Luminescent CuInS<sub>2</sub>/ZnS Core/Shell Nanocrystals: Cadmium-Free Quantum Dots for In Vivo Imaging. *Chem. Mater.* **2009**, *21*, 2422–2429.
- (41) Fu, M.; Luan, W.; Tu, S.-T.; Mleczko, L. Green Synthesis of CuInS<sub>2</sub>/ZnS Nanocrystals with High Photoluminescence and Stability. *J. Nanomater.* **2015**, *2015*, 1–9.
- (42) Dabbousi, B. O.; Rodriguez-Viejo, J.; Mikulec, F. V.; Heine, J. R.; Mattoucci, H.; Ober, R.; Jensen, K. F.; Bawendi, M. G. (CdSe)ZnS Core–Shell Quantum Dots: Synthesis and Characterization of a Size Series of Highly Luminescent Nanocrystallites. *J. Phys. Chem. B* **1997**, *101*, 9463–9475.
- (43) Kuo, K.-T.; Chen, S.-Y.; Cheng, B.-M.; Lin, C.-C. Synthesis and Characterization of Highly Luminescent CuInS<sub>2</sub> and CuInS<sub>2</sub>/ZnS (Core/Shell) Nanocrystals. *Thin Solid Films* **2008**, *517*, 1257–1261.
- (44) Wang, Y.; Guo, S.; Luo, H.; Zhou, C.; Lin, H.; Ma, X.; Hu, Q.; Du, M.; Ma, B.; Yang, W.; Lü, X. Reaching 90% Photoluminescence Quantum Yield in One-Dimensional Metal Halide C 4 N 2 H 14 PbBr 4 by Pressure-Suppressed Nonradiative Loss. *J. Am. Chem. Soc.* **2020**, *142*, 16001–16006.
- (45) Tolbert, S. H.; Alivisatos, A. P. Size Dependence of the Solid–Solid Phase Transition in CdSe Nanocrystals. *Z. Phys. D: At., Mol. Clusters* **1993**, *26*, 56–58.
- (46) González, J.; Rincón, C. Optical Absorption and Phase Transitions in CuInSe<sub>2</sub> and CuInS<sub>2</sub> Single Crystals at High Pressure. *J. Appl. Phys.* **1989**, *65*, 2031–2034.
- (47) Tinoco, T.; Polian, A.; Gómez, D.; Itié, J. P. Structural Studies of CuInS<sub>2</sub> and CuInSe<sub>2</sub> under High Pressure. *Phys. Status Solidi B* **1996**, *198*, 433–438.
- (48) Sapra, S.; Sarma, D. D. Evolution of the Electronic Structure with Size in II–VI Semiconductor Nanocrystals. *Phys. Rev. B: Condens. Matter Mater. Phys.* **2004**, *69*, 125304.
- (49) Zhao, H.; Yin, H.; Liu, X.; Li, H.; Shi, Y.; Liu, C.; Jin, M.; Gao, J.; Luo, Y.; Ding, D. Pressure-Induced Tunable Electron Transfer and Auger Recombination Rates in CdSe/ZnS Quantum Dot-Anthraquinone Complexes. *J. Phys. Chem. Lett.* **2019**, *10*, 3064–3070.
- (50) Yuan, C. T.; Lin, Y. C.; Chen, Y. N.; Chiu, Q. L.; Chou, W. C.; Chu, D. S.; Chang, W. H.; Lin, H. S.; Ruaan, R. C.; Lin, C. M.
- Studies on the Electronic and Vibrational States of Colloidal CdSe/ZnS Quantum Dots under High Pressures. *Nanotechnology* **2007**, *18*, 185402.
- (51) Félix, G.; Mikolasek, M.; Molnár, G.; Nicolazzi, W.; Bousseksou, A. Control of the Phase Stability in Spin-Crossover Core–Shell Nanoparticles through the Elastic Interface Energy. *Eur. J. Inorg. Chem.* **2018**, *2018*, 435–442.
- (52) Wu, B.; Lu, W. Mechanical Modeling of Particles with Active Core–Shell Structures for Lithium-Ion Battery Electrodes. *J. Phys. Chem. C* **2017**, *121*, 19022–19030.
- (53) Hawa, T.; Zachariah, M. R. Internal Pressure and Surface Tension of Bare and Hydrogen Coated Silicon Nanoparticles. *J. Chem. Phys.* **2004**, *121*, 9043–9049.

## □ Recommended by ACS

### Low-Temperature Photoluminescence Dynamics Reveal the Mechanism of Light Emission by Colloidal CuInS<sub>2</sub> Quantum Dots

Małgorzata Szymura, Łukasz Kłopotowski, et al.

MARCH 30, 2023

THE JOURNAL OF PHYSICAL CHEMISTRY C

READ ▶

### Facile High-Yield Synthesis of Ag–In–Ga–S Quaternary Quantum Dots and Coating with Gallium Sulfide Shells for Narrow Band-Edge Emission

Taro Uematsu, Susumu Kuwabata, et al.

JANUARY 19, 2023

CHEMISTRY OF MATERIALS

READ ▶

### Optically Detected Magnetic Resonance Spectroscopy of Cu-Doped CdSe/CdS and CuInS<sub>2</sub> Colloidal Quantum Dots

Adi Harchol, Efrat Lifshitz, et al.

AUGUST 01, 2022

ACS NANO

READ ▶

### Wurtzite InAs Nanocrystals with Short-Wavelength Infrared Emission Synthesized through the Cation Exchange of Cu<sub>3</sub>As Nanocrystals

Xinyao Shan, Botao Ji, et al.

MARCH 06, 2023

CHEMISTRY OF MATERIALS

READ ▶

Get More Suggestions >